Check for updates

Advanced Materials Technologies

ADVANCED MATERIALS TECHNOLOGIES
www.advmattechnol.com

RESEARCH ARTICLE

Thin-Film MoS_2 Phototransistor-Integrated Piezo-Transmittance Sensor for Wearable Electronics

Jimin Gu[1] | Injun Lee[1] | Seok-Young Ji[2] | Junseong Ahn[3] | Jungrak Choi[4] | Yongrok Jeong[5] | Ji-hwan Ha[6] | Won Seok "Paul" Chang[2] | Byeong-Soo Bae[1] | Inkyu Park[1]

[1]Department of Mechanical Engineering, Korea Advanced Institute of Science and Technology (KAIST), Daejeon, Republic of Korea | [2]Department of Nano Manufacturing Technology, Korea Institute of Machinery and Materials (KIMM), Daejeon, Republic of Korea | [3]Department of Control and Instrumentation Engineering, Korea University, Sejong, Republic of Korea | [4]Electronics and Telecommunications Research Institute (ETRI), Daejeon, Republic of Korea | [5]School of Mechanical Engineering, Kyungpook National University, Daegu, Republic of Korea | [6]Department of Mechanical Engineering, Hanbat National University, Daejeon, Republic of Korea

Correspondence: Won Seok "Paul" Chang (paul@kimm.re.kr) | Byeong-Soo Bae (bsbae@kaist.ac.kr) | Inkyu Park (inkyu@kaist.ac.kr)

Received: 16 September 2025 | **Revised:** 6 April 2026 | **Accepted:** 27 April 2026

Keywords: femtosecond laser cutting | MoS_2 thin film-based phototransistor | piezo-transmittance | strain sensors | wearable strain sensors

ABSTRACT

Soft and stretchable wearable sensors are increasingly critical for healthcare diagnostics, sports performance monitoring, and virtual/augmented reality. Piezo transmittance sensors offer several key advantages, including fast response time, high sensitivity, long-term durability, and self-powered operation through ambient light. However, they are often limited by their bulkiness and the difficulty of fabrication of flexible optical components, hindering their stretchability. We introduce a design strategy to miniaturize and ensure stretchability to piezo-transmittance strain sensors. The MoS_2-based phototransistor, fabricated on a flexible polyimide substrate, offers mechanically compliant visible light detection, yielding a fully flexible optical sensing element. By integrating serpentine-patterned electrodes with a nanocomposite piezo transmittance layer, we developed a highly conformable wearable sensor platform. This sensor exhibits stable optical responsiveness up to 20% strain and leverages ambient light. The sensor was successfully integrated onto the wearable platform and demonstrates its effectiveness of tracking the sports performance during weighted workout, such as seated bench presses and arm curls.

1 | Introduction

In recent years, wearable sensors made from soft, compliant materials have garnered significant attention owing to their various applications in healthcare [1–4], sports monitoring [5–7], and virtual/augmented reality (VR/AR) systems [8–10]. Among these, strain sensors, which measure the deformation of target objects, are particularly important. They play a critical role in monitoring joint movement and muscle activity, which is essential for sports performance analysis and healthcare applications. Among the various types of soft strain sensors, piezo-transmittance strain sensors, which operate using the changes in optical transmittance, stand out owing to their minimal hysteresis, low drift, high reliability, and stability. Their principle relies on a stretchable elastomer-based composite film that changes its visible light transmittance, allowing strain to be measured by variations in the light intensity. The first piezo-transmittance strain sensor, developed in 2017 [11], used a TiO_2-elastomer composite film. However, the thorough sensor performance characterization was limited. In 2020 [12], further studies on these sensors using carbon nanotube (CNT)-elastomer composites highlighted their promising features. Follow-up research focused on addressing challenges related to uniformity and design flexibility [13].

© 2026 Wiley-VCH GmbH

Despite advances in the development of piezo-transmittance strain sensors, bulkiness in the overall system remains a key limitation. The operating principle of these sensors involves detecting changes in light transmittance in the functional layer when strain is applied, requiring both a functional layer and a detection layer to measure the light intensity change. While these sensors demonstrate strong performance and potential for green energy applications, such as integration with solar cells or low-energy photodetectors, their flexibility is restricted by the non-stretchable or rigid platforms used, particularly when solar cells are integrated.

Although this arrangement works well for structural health monitoring, it can impede movement when applied as a wearable sensor. To address this, a phototransistor was fabricated on a flexible polyimide substrate patterned in a serpentine geometry to enable stretchability. The sensor integrates molybdenum disulfide (molybdenum (IV) sulfide, MoS_2)-based thin-film phototransistors with nanocomposite piezo-transmittance films.

Unlike a two-terminal photoconductor, a phototransistor incorporates a gate electrode that enables active control of the channel carrier concentration, allowing dark current to be suppressed and the signal-to-noise ratio to be improved [14]. Gate bias also modulates the channel mobility and photoconductive gain, enabling continuous tuning of responsivity across a wide range without modifying the device structure [15]. This tunability allows the operating point to be optimized for linearity and stability, which is particularly important for accurate strain transduction in wearable sensing applications.

The implementation of 2D materials as photodetectors has been widely explored because of their exceptional property of possessing a high light absorption coefficient compared to their thickness. Graphene-based photodetectors exhibit low responsivity due to high dark current, which arises from the absence of a bandgap. In contrast, transition metal dichalcogenides (TMD) possess a honeycomb structure akin to graphene and a bandgap advantage. This key feature of TMD results in a smaller dark current than graphene, making them promising materials for optical devices, as demonstrated by many previous studies [16, 17]. Among them, MoS_2 is noteworthy, owing to its remarkable characteristics, such as a high current on-off ratio, high carrier mobility, and efficient light absorption in the visible spectrum range. Furthermore, this material exhibits atomic thickness with a direct bandgap, which varies with thickness, transitioning from indirect to direct as it becomes thinner, making it highly desirable as a photodetector for its superior photosensitive properties [18]. Its unique features, including mechanical flexibility, transparency, and biocompatibility, also make it ideal for wearable sensors [19, 20]. The wafer-scale MoS_2 was synthesized using chemical vapor deposition (CVD) method, [21] followed by wet transfer method to a target substrate for integration into a photodetector. In this study, the exceptional properties of MoS_2 were harnessed to manufacture a low-power photodetection layer that specifically targets visible wavelength (λ = 380–700 nm). The sensor consists of two layers: a piezo-transmittance (PT) layer and a light detection (LD) layer. The PT layer, made from a CNT-elastomer composite, changes its optical transmittance when strained. The LD layer then measures the light transmitted through the PT layer. The sensor's design incorporates island and serpentine structures to ensure it can withstand various deformations. MoS_2, chosen for its excellent light absorption in the visible spectrum, was used as the photodetector material on a polyimide (PI) substrate, which offers mechanical strength and electrical insulation. The fabrication conditions, including atomic layer deposition (ALD) temperature and channel length, were optimized to improve the photodetection performance of the MoS_2 phototransistor for wearable applications. The serpentine structure was also carefully analyzed to enhance the mechanical stretchability of the thin-film phototransistor. The sensor was tested in a wearable workout monitoring system, where it successfully tracked performance and movements during seated bench press and arm curl exercises.

2 | Results and Discussion

The overall structure of the sensor is shown in Figure 1a, composed of two different layers; the PT layer and the LD layer. The PT layer allows light to pass through and its transmittance changes in response to external tensile strain. The light then travels to the LD layer where the quantity of light is measured. The PT layer is based on a composite of CNT and elastomer, the CNT film in the PT layer undergoes crack growth upon tensile deformation, leading to an increase in the transmittance of light through the opened cracks, as depicted in Figure 1b.

The serpentine structure makes the PI film stretchable, ensuring that the optical devices in the center part do not suffer from mechanical failure caused by external strain. The central area of PT part is designed to elongate to enhance crack opening, while being mechanically decoupled from the LD layer to prevent stress on the detector area. This design ensures that tensile stress is concentrated on the PT layer, without affecting the LD layer detector's stability.

The detail design and fabrication of MoS_2 phototransistor layer are critical in a piezo-transmittance strain sensor. A thin film phototransistor was constructed using a combination of MoS_2 and PI substrate. The proposed system employs PI as a substrate for mechanical strength and electrical insulation while exposed to various stretching degrees.

The structure of the fabricated MoS_2-based thin-film phototransistor is shown in Figure 1c, and the manufacturing process is illustrated in Figure 1d. The substrate is a polyimide layer, which ensures flexibility. The gate electrode and source-drain electrodes are deposited, with the MoS_2 photoactive layer positioned at the center. The final passivation layer is composed of alumina. Each layer's material and function in the phototransistor are indicated. To create the flexible substrate, pre-polymer PI was spin-coated onto a 4-inch silicon wafer with Poly(Methyl Methacrylate) (PMMA) as the sacrificial layer (Figure 1d-i,ii). Subsequently, an alumina buffer layer (Al_2O_3) was deposited (Figure 1d-iii), followed by the deposition of the gate electrode with Au (Figure 1d-iv). The gate insulator layer was fabricated using ALD process (Figure 1d-v). MoS_2 was grown according to the literature [22], demonstrating exceptional spatial homogeneity, and high electrical performance. The MoS_2 was

2365709x, 2026, 16, Downloaded from https://advanced.onlinelibrary.wiley.com/doi/10.1002/admt.202501979 by Korea University Library, Wiley Online Library on [22/09/2026]. See the Terms and Conditions (https://onlinelibrary.wiley.com/terms-and-conditions) on Wiley Online Library for rules of use; OA articles are governed by the applicable Creative Commons License

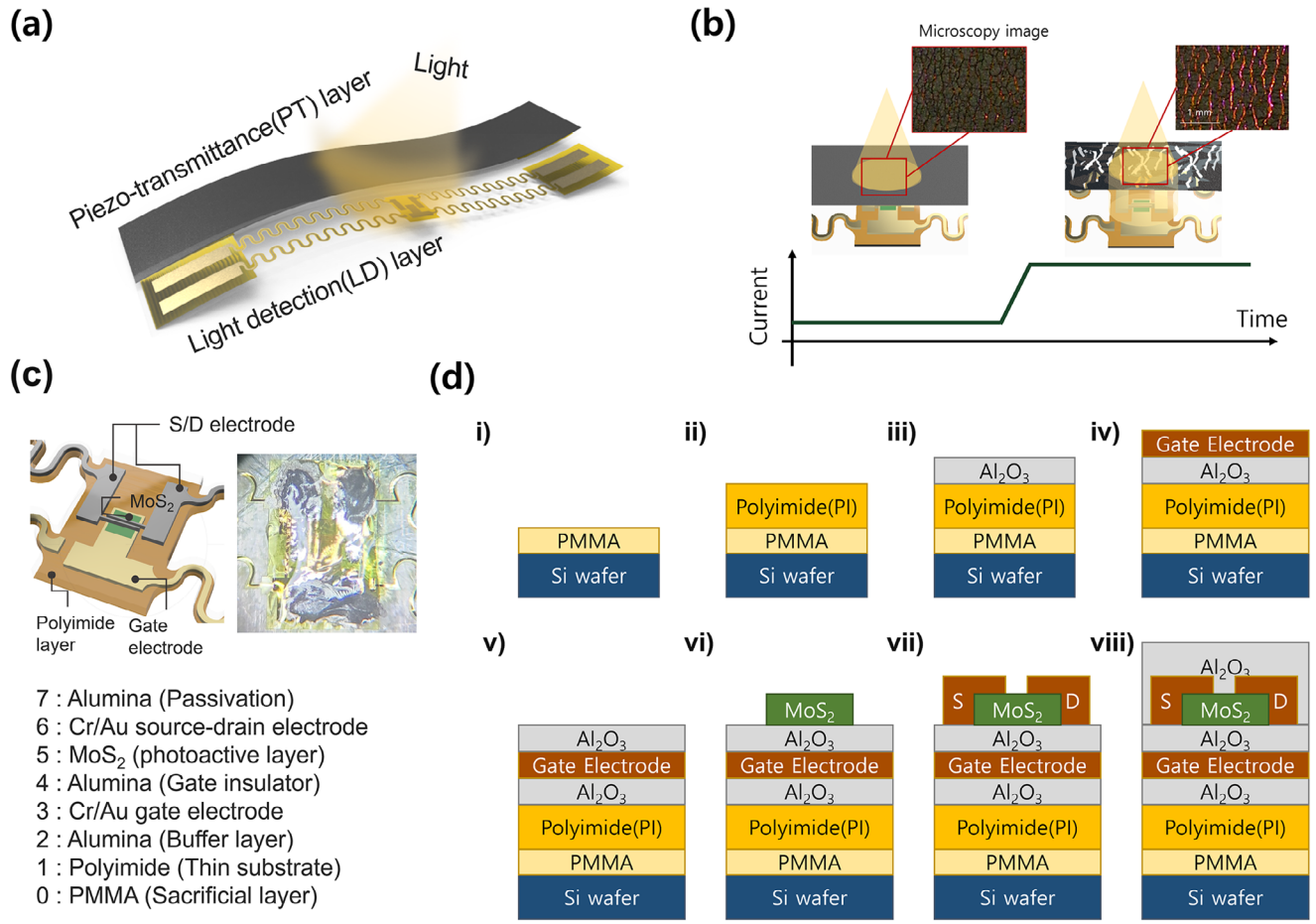


FIGURE 1 | Overview of the thin film-based piezo-transmittance strain sensor and its stretching characteristics: (a) Structure and component of proposed sensor. (b) Sensing mechanism. (c) Overview structure of the flexible MoS_2 phototransistor and microscopic image. (d) Fabrication Process of proposed MoS_2 phototransistor (i) spin-coated PMMA solution onto the 4 inch Si wafer (ii) spin-coated and curing the polyimide(PI) (iii) deposited alumina as a buffer layer (iv) deposited Cr/Au layer as a gate electrode (v) deposited alumina as gate insulator (vi) wet transfer of MoS_2 as a photoactive layer (vii) deposited Cr/Au layer as source-drain electrodes (viii) deposited alumina as a passivation layer. (e) Photograph of the piezo-transmittance layer and integrated system. (i) CNT film stretching behavior in $\varepsilon = 0\%$ and 30%. (ii) Detection layer stretching behavior in $\varepsilon = 0\%$ and 30%. (iii) Sideview and the stretching behavior of the whole integrated system. (f) Various deformations of the sensor: stretching, twisting, and bending.

then transferred onto the target substrate via the wet transfer method (Figure 1d-vi), using a PMMA carrier film, which was later dissolved with acetone. The source and drain electrodes were then deposited (Figure 1d-vii) using the same method as the gate electrode. The MoS_2 layer was encapsulated with a high-k Al_2O_3 layer by the ALD process as the final step (Figure 1d-viii).

Figure 2a-i shows that the region of highest elongation within the film is the center, as demonstrated by the central area consisting solely of the CNT layer and the Ecoflex layer. To ensure the central part stretches more easily, the film is designed with only the low compliance CNT-Ecoflex layer, while the sides are reinforced with an additional PDMS layer which has high compliance, to restrict their elongation. This created a compliance difference between the central and peripheral areas, concentrating the elongation in the center. The fabrication process for the CNT/Ecoflex elastomer layer is detailed in Figure S1 and the Methods section. Conversely, stretching in the LD layer (Figure 2a-ii) shows minimal strain in the center, where the MoS_2 phototransistor is located. Although the detector positions experience minor strain in the LD layer, the movement between the LD and stretchable PT layers must be decoupled, as shown in Figure 2a-iii. Therefore, as described in Figure S2 and the Methods section, a decoupling layer was added, along with a silicone lubricant between the LD and PT layers, to package the entire structure into one sensor system. Finally, the packaged strain sensor for wearable applications was exposed to various deformations, such as stretching, twisting, and bending, demonstrating its ability to withstand these deformations (Figure 2b).

Two fabrication parameters were investigated to characterize their influence on the responsivity and response time of the phototransistor, which is ALD process temperature and channel length. The electrical characteristics and photoresponsivity of the fabricated phototransistors are consistent with values reported in the literature [23]. Responsivity, detectivity, and response time are essential performance indexes in phototransistors. Responsivity and detectivity are defined as follows.

$$\text{Responsivity} = \frac{I_{photo}}{P_{light}}$$

2365709x, 2026, 16, Downloaded from https://advanced.onlinelibrary.wiley.com/doi/10.1002/admt.202501979 by Korea University Library, Wiley Online Library on [22/09/2026]. See the Terms and Conditions (https://onlinelibrary.wiley.com/terms-and-conditions) on Wiley Online Library for rules of use; OA articles are governed by the applicable Creative Commons License

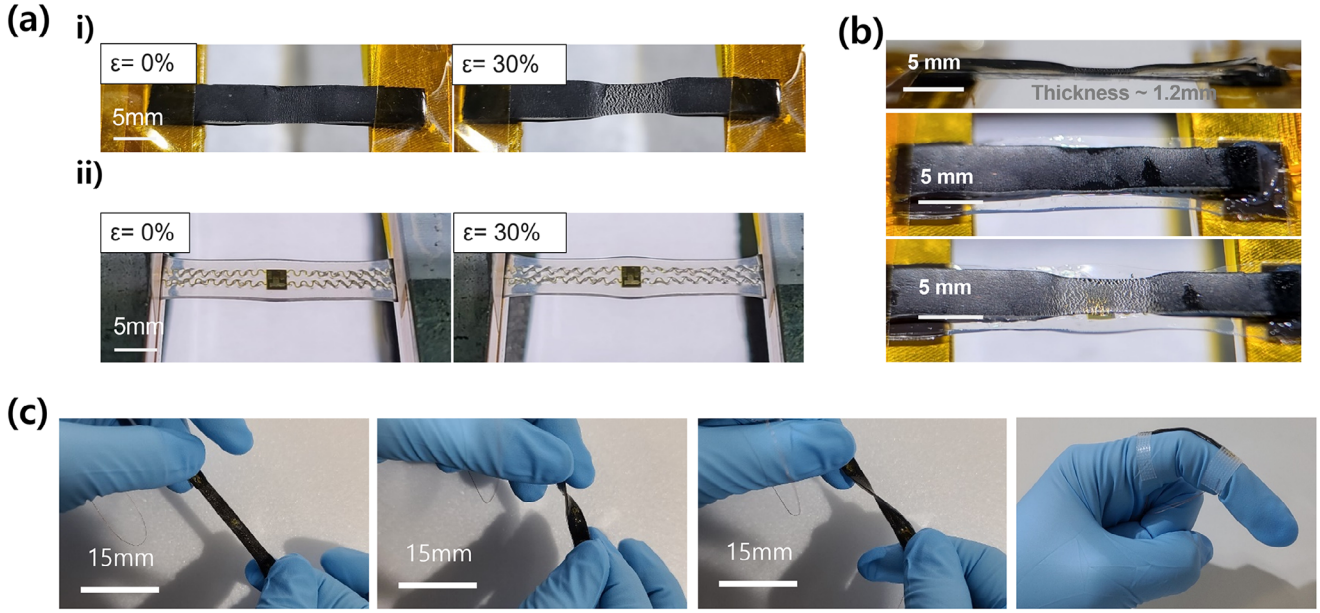


FIGURE 2 | Photograph of the piezo-transmittance layer and integrated system: (a) CNT film stretching behavior in $\varepsilon = 0\%$ and 30%. (b) Detection layer stretching behavior in $\varepsilon = 0\%$ and 30%. (c) Various deformations of the sensor: stretching, twisting, and bending.

$$\text{specific Detectivity} = \text{Responsitivty} \times \sqrt{\frac{A}{2eI_{dark}}}$$

where I_{photo} is photo current, P_{light} is the power of incident light, A is the area of the photodetector e is the electric charge, and I_{dark} is the dark current. The response time is defined as the time required for the output to reach from 10% to 90% of its final saturated values. The expression D* is an established convention in the MoS_2 photodetector literature for reporting the theoretical upper bound of detectivity and enabling consistent comparison across studies [20]. The reported D* values in this work (1.17×10^{10} Jones at $\lambda = 520$ nm and 7.57×10^{9} Jones at $\lambda = 630$ nm, at $V_{DS} = 5$ V and $V_{GS} = 10$ V) are adopted under this same convention and should be interpreted as theoretical upper-bound estimates.

From this equation, the photocurrent directly affects the performance significantly, and the response time is greatly affected by the electron mobility of the material itself.

The ALD temperature of Al_2O_3 used as a passivation layer affects responsivity because the encapsulation of CVD-grown MoS_2 with high-k Al_2O_3 suppresses Coulomb and phonon scattering caused by defects and trap states, thereby improving the material's mobility [24]. Minimizing interface defects between the 2D active channel layer and the metal electrode can improve reliability by reducing the trapping of photogenerated carriers in these defects that can cause high contact resistance and degrade photosensor performance. The Al_2O_3 layer also removes surface adsorbates, enhancing the overall quality of the MoS_2. Based on these advantages, the passivation layer process was added last, and it was experimentally confirmed that the process temperature affects the sensor's performance.

As illustrated in Figure 3a, increasing the temperature of the ALD process during the deposition of the aluminum layer, which serves as a passivation and gate insulation layer, enhances photocurrent reactivity. However, when the process temperature exceeds 250°C, responsivity no longer improves and appears to reach saturation. Higher ALD process temperatures correlate with better recovery performance and increased photocurrent. This phenomenon can be explained by two factors. First, elevated ALD temperatures reduce the likelihood of electron trapping in the gate insulation and passivation layers, resulting in decreased interface defect density. Second, higher ALD temperatures enhance the carrier concentration in MoS_2, further increasing photocurrent.

The second factor investigated is the channel length, defined as the distance between the source and drain electrodes. Experimental results presented in Figure 3b, obtained at channel lengths of 20, 30, 40, and 50 μm, demonstrate that as channel length increases, photocurrent decreases, leading to a significant reduction in responsivity. However, longer channel lengths exhibit a minor drift phenomenon, suggesting improved recovery time.

Short channel lengths result in low contact resistance, high photocurrent, and a greater likelihood of electron trapping in the gate insulation and passivation layers. In contrast, longer channel lengths decrease photocurrent while improving recovery time, ultimately reducing responsivity. The dynamic recovery characteristics for channel lengths of 30, 40, and 50 μm are illustrated in Figure 3c,d. Figure 3c shows how the phototransistor measures changes in transmittance of the PT layer when strain is continuously increased by 10%–20% and then reduced. Figure 3d demonstrates the recovery behavior when strains of 10%, 20%, 40%, 60%, 80%, and 100% are applied and subsequently released. Given that phototransistors primarily measure physical indicators, recovery time takes precedence over responsivity.

2365709x, 2026, 16, Downloaded from https://advanced.onlinelibrary.wiley.com/doi/10.1002/admt.202501979 by Korea University Library, Wiley Online Library on [22/09/2026]. See the Terms and Conditions (https://onlinelibrary.wiley.com/terms-and-conditions) on Wiley Online Library for rules of use; OA articles are governed by the applicable Creative Commons License

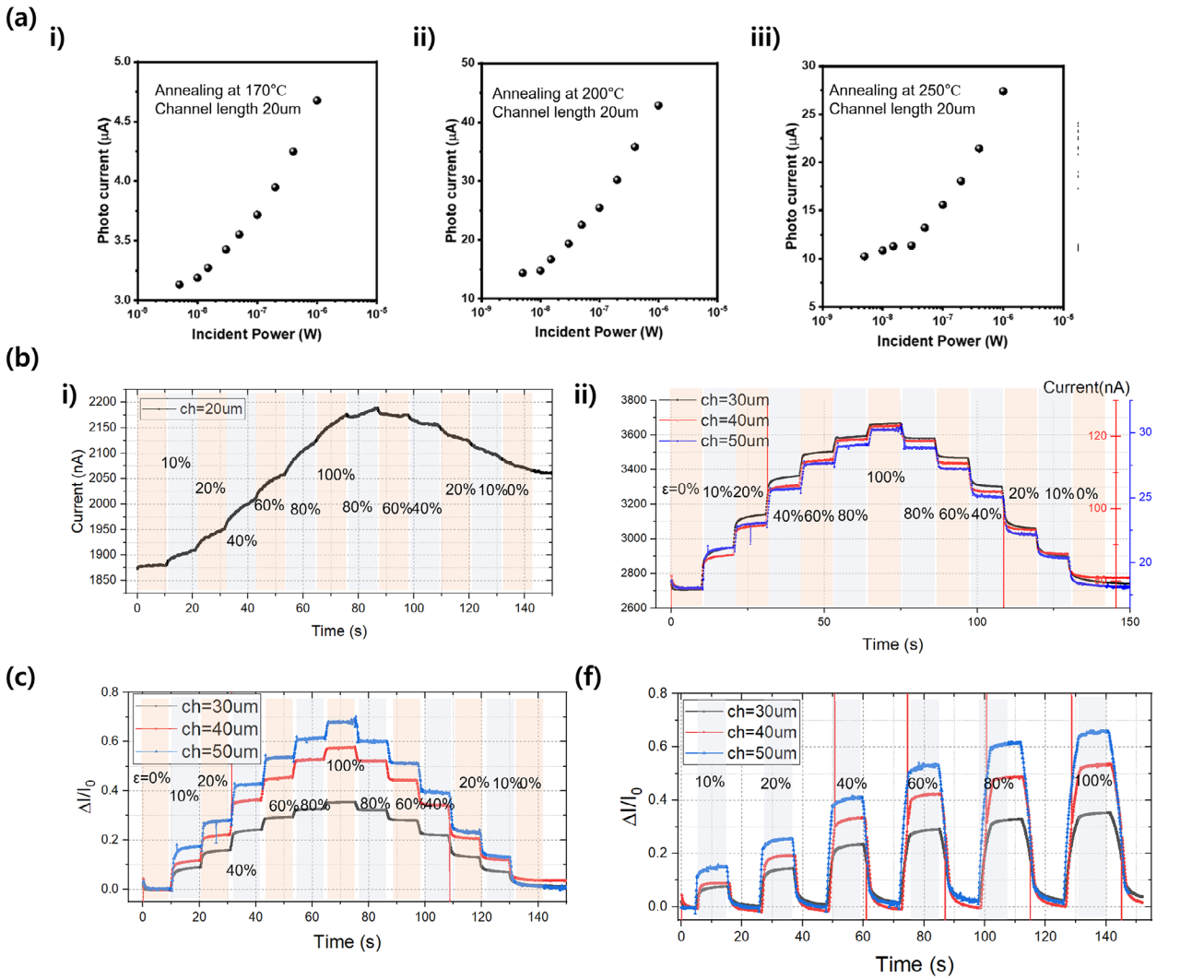


FIGURE 3 | Fabrication factors affecting the performance of phototransistors. (a) Effect of the annealing temperature on the sensor performance. The responsivity of the MoS2-based flexible photodetector according to the incident light power with annealing temperature of (i) T = 170°C, (ii) T = 200°C, (iii) T = 250°C. (b) Photocurrent response according to the incident light power with channel length of (i) L = 20 μm, (iii) L = 30, 40 and 50 μm (c) Measurement of transmittance changes in the PT layer as the strain is continuously increased by 10%–20% and subsequently reduced. (d) Dynamic recovery behavior of the phototransistor under applied strains of 10%, 20%, 40%, 60%, 80%, and 100%.

Therefore, the ALD process temperature is precisely set at 200°C, and a channel length of 50 μm is employed to assess the change in light transmittance of CNTs, ensuring optimal recovery properties while maintaining satisfactory responsivity.

To reduce strain concentration on the island while providing stretchability to the LD layer, the serpentine electrode was designed based on the material's mechanical properties. A study on the mechanical stretching stability of the fabricated MoS_2-based thin-film phototransistor was particularly focused on Al_2O_3, the stiffest and most brittle material among the film structures. According to the literature, the maximum strain for Al_2O_3 to avoid mechanical damage should be less than 1% [25]. In addition to Al_2O_3, the strain applied to PI and Au was also assessed. Therefore, to create a structure capable of a high tensile of 20%–30%, a large strain should not be applied to the island where the phototransistor is located. To this end, the structure shown in Figure 4a was designed by combining the island and serpentine structures.

The literature indicates that stretchability varies depending on the geometric parameters of the serpentine design, such as ribbon width, arc radius, arm length, and substrate support. Specifically, the smaller the width of the serpentine, the higher the stretchability. However, the width cannot be zero in practice; as the width decreases and the serpentine length increases, the electrode resistance associated with the serpentine also increases, reducing sensing performance. In the integrated sensor, the serpentine electrode should have a width of 100 μm or larger, and consequently, the PI serpentine pattern should have a width of 200 μm or more. This specification is necessary to prevent damage to the electrode during the femtosecond laser cutting process. To ensure sufficient clearance and avoid electrode damage, a safety factor of 2 has been applied, resulting in a minimum width of 200 μm for the PI pattern. While the femtosecond laser system provides resolution well below 50 μm, an additional clearance is maintained to ensure safe operation. If the strain applied externally is ε_{app} and the maximum strain experienced by the structure is ε_{max}, this ratio, referred to as 'gain' from now on, can

2365709x, 2026, 16, Downloaded from https://advanced.onlinelibrary.wiley.com/doi/10.1002/admt.202501979 by Korea University Library, Wiley Online Library on [22/09/2026]. See the Terms and Conditions (https://onlinelibrary.wiley.com/terms-and-conditions) on Wiley Online Library for rules of use; OA articles are governed by the applicable Creative Commons License

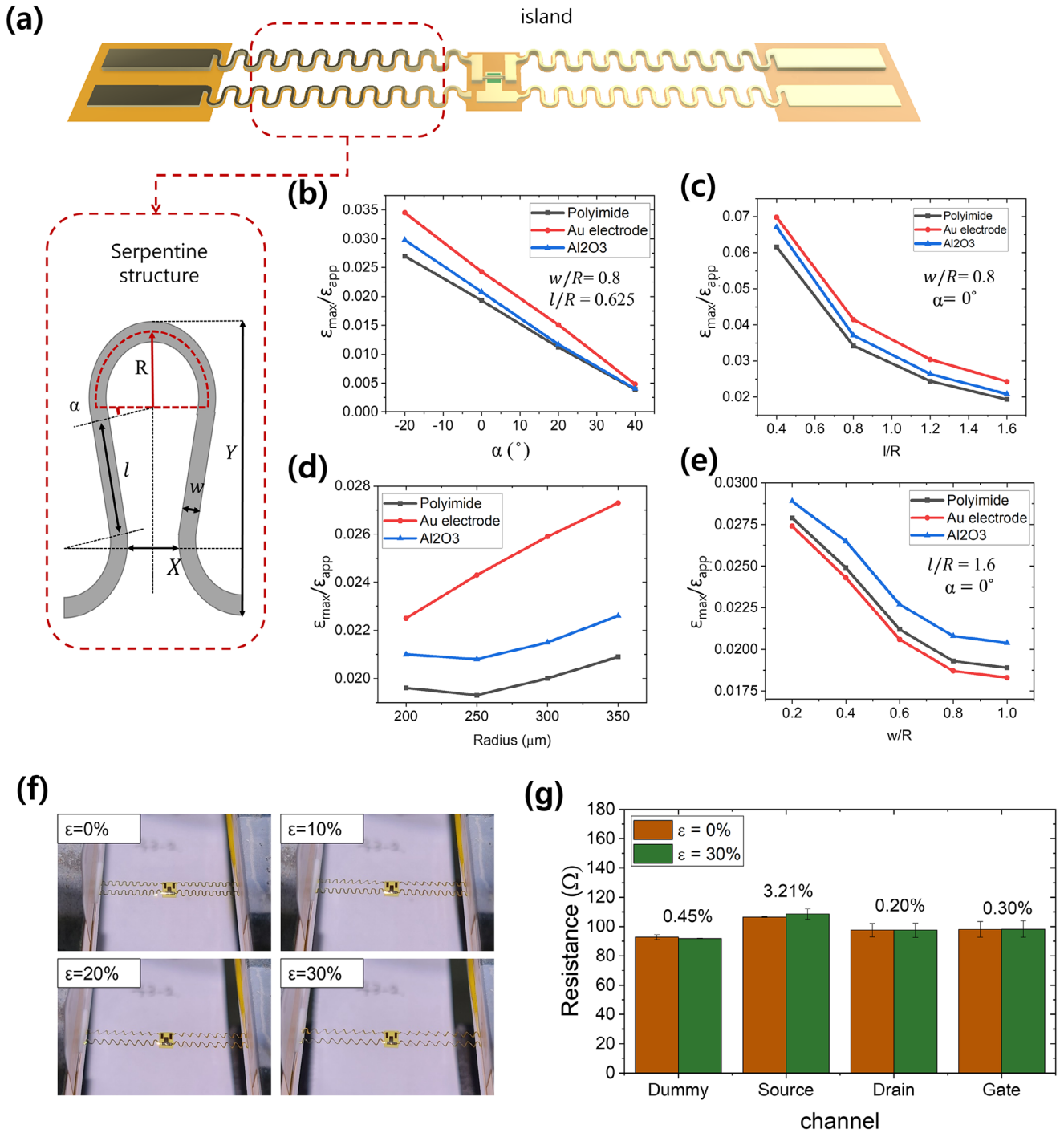


FIGURE 4 | Design of stretchable LD layer and their mechanical stability characteristics: (a) LD layer with serpentine electrode structure for reducing the stress concentration on the detection area and larger stretchability. Parametric calculation of the $\varepsilon_{max}/\varepsilon_{app}$ for different parameters. (b) Effect of the serpentine angle alpha. (c) Effect of the ratio of the length of the serpentine and the radius of the serpentine (l/R). (d) Effect of the radius of the serpentine. (e) Effect of the width and radius ratio of the serpentine (w/R). (f) Illustration of sensor stretching and the deformation of the serpentine electrode under various applied strains. (g) Measurement of resistance changes during stretching, demonstrating that the resistance variation remains below 5% for all electrodes, validating the stability of the serpentine structure.

2365709x, 2026, 16, Downloaded from https://advanced.onlinelibrary.wiley.com/doi/10.1002/admt.202501979 by Korea University Library, Wiley Online Library on [22/09/2026]. See the Terms and Conditions (https://onlinelibrary.wiley.com/terms-and-conditions) on Wiley Online Library for rules of use; OA articles are governed by the applicable Creative Commons License

be expressed as follows, according to the literature [26].

$$\frac{\varepsilon_{max}}{\varepsilon_{app}} = \frac{\frac{w}{R}\left[\frac{12}{2-\frac{w}{R}} + \left(\frac{12}{2-\frac{w}{R}} - \frac{w}{R}\right)(\sin\alpha + \frac{l}{2R}\cos\alpha)\right]\left(\cos\alpha - \frac{l}{2R}\sin\alpha\right)}{\cos^2\alpha\left(\frac{l^3}{2R^3} + 3\left(\frac{\pi}{2}+\alpha\right)\frac{l^2}{R^2} + 12\frac{l}{R} - 12\left(\frac{\pi}{2}+\alpha\right)\right)}$$

$$+\sin 2\alpha\left(6\left(\frac{\pi}{2}+\alpha\right)\frac{l}{R}+9\right) + \frac{w^2}{R}\left[\left(\frac{\pi}{2}+\alpha\right)\left(\frac{l}{2R}\cos\alpha + \sin\alpha\right)^2\right.$$

$$\left.+\frac{l}{2R}(\sin\alpha + \frac{3E}{2G}\cos\alpha)\right] + 18\left(\frac{\pi}{2}+\alpha\right)$$

where the w is the width of the serpentine, R is the arc radius, α is the arc angle, and l is the arm length. The smaller this ratio is, the smaller the maximum strain applied to the structure compared to the external tension, so stretching is possible in a wider range.

Figure 4b–e shows the results of the $\varepsilon_{max}/\varepsilon_{app}$ ratio applied to the polyimide, gold, and Al_2O_3 used in this paper in the serpentine structure. As can be seen in the graph, the larger the angle (α) of the serpentine structure, the greater the maximum strain. On the other hand, when X is the distance in the x direction from a serpentine ribbon to the next ribbon, X is as follows.

$$X = \left(R - \frac{w}{2}\right)cos\alpha - l\,sin\alpha - \left(R + \frac{w}{2}\right)(1 - cos\alpha)$$

This value should be greater than 100 μm due to process limitations. In Figure 4b, the larger the α angle of the serpentine pattern, the better. However, when X is calculated under the given conditions, α must have a value of 6.5° or less. Here, $\alpha = 0°$ was chosen for ease of fabrication. The larger the value of l/R, the greater the strain, but the longer l is, the longer the length of the electrode, and the greater the resistance accordingly. In this work, l = 400 μm was set. A larger w/R results in a decrease in the gain term ($\frac{\varepsilon_{max}}{\varepsilon_{app}}$) for the Al_2O_3 and PI layers, implying that as the gain term decreases, the structure can endure higher strains relative to the applied strain, as shown in Figure 4e. According to the above calculation, the PI layer was cut with R = 250 μm, l = 400 μm, and w = 200 μm. When the fabricated serpentine and island structures were exposed to various mechanical stimuli, the von Mises stress and maximum volume strain applied to the islands were analyzed through the finite element method (FEM). FEM simulation results can be analyzed based on the volumetric strain of the structure reaching the failure strain. The FEM simulation was conducted for PI, which is the main substrate, and Al_2O_3, which has the highest stiffness and is likely to fail. The failure strain of PI varies slightly depending on the manufacturer and processing method, but according to the literature [25], the failure strain is about 6.4%, while that of Al_2O_3 is about 1%. The volumetric strain applied to the structure when ε = 0%–20% is applied using the COMSOL solid mechanics module is shown in Figure S3a,b for PI and Al_2O_3, respectively. The maximum volumetric strain value in each strain region is shown in Figure S3c, and the local maximum volumetric strain value of the structure is smaller than the failure strain region of each material based on this criterion, so it can be confirmed by simulation that the structure can be utilized in the ε = 0–20% region without significant damage to the phototransistor region. The sensor stretching and the deformation of the serpentine electrode for each applied strain are depicted in Figure 4f. To validate the stretchability and stability achieved by the serpentine structure, the change in resistance during stretching was measured and is shown in Figure 4g, where the resistance change remains below 5% for all electrodes.

Figure 5a shows the photocurrent response of the MoS_2 phototransistor as the incident light intensity increases from 0.04 to 0.07 W/cm^2, measured at V_g = 1 V and V_{ds} = 5 V. The photocurrent exhibits a linear dependence on light intensity, with a responsivity of 93.12 nA/(W/cm^2). This linear relationship establishes the quantitative link between the microstructural evolution of the CNT layer and the electrical output of the device: strain-induced opening of the CNT network increases optical transmittance (Figure 1b), and the linearity shown here confirms that this transmittance change is directly and accurately transduced into a measurable photocurrent. The response of the MoS_2 phototransistor to both light intensity and strain varies with gate and source-drain voltage, and the corresponding results are shown in Figure 5b. The integrated sensor was characterized at V_g = 1 V and V_{ds} = 5 V, as these conditions produced the most linear and stable strain response. Figure S5a presents the detection limit (LOD = $3S_b$/b) of the sensor, determined by applying a 2% strain step input repeatedly. The calculated value of the LOD, based on the above equation, is 0.73% as depicted on Figure 5c. Figure 5d shows the current change based on the phototransistor current of 0% when the strain is increased by 2.5% and held for 5 s, where I_0 is the source-drain current at strain = 0% and ΔI is the difference between the source-drain current I at that strain subtracted from I_0. The response of the sensor is plotted as a strain-response based on the average value of each 5 s holding interval. As shown in Figure 5e, the sensor exhibits a gauge factor (G.F) of 2 in response to the strain input; however, noise is observed during the holding phase due to the inherent response time limitation of the phototransistor.

Figure 5f depicts the cyclic stability of the sensor response under two experimental conditions. In the first condition, 100 loading–unloading cycles were applied with a 5-s hold at each strain level within the ε = 0%–20% range. As presented in Figure S4b, 100 cycles were applied continuously without a hold period. The results show that under continuous dynamic loading without a hold, the sensor output does not fully return to its baseline value between cycles, which can be attributed to the finite response time inherent to the device. In contrast, when a sufficient hold time is applied, the sensor accurately resolves static strain inputs, indicating that the response time limitation does not affect quasi-static measurement fidelity. Simulation results further confirm that the island-serpentine architecture effectively decouples macroscopic substrate deformation from the active sensing region, constraining local strain at the MoS_2 phototransistor to below 0.1%. This structural decoupling mitigates mechanical fatigue accumulation in the rigid semiconductor layer under repeated deformation.

Environmental stability during skin-interfaced operation is addressed through a dual-layer encapsulation strategy. The primary barrier consists of a dense Al_2O_3 film deposited by atomic layer deposition (ALD), which conformally encapsulates the MoS_2 channel. Due to its pinhole-free morphology and low water vapor transmission rate [27], the ALD-grown Al_2O_3 layer effectively impedes moisture ingress and ion transport associated with sweat exposure. The secondary barrier is provided by the PDMS matrix, which is chemically inert and hydrophobic, and in

2365709x, 2026, 16, Downloaded from https://advanced.onlinelibrary.wiley.com/doi/10.1002/admt.202501979 by Korea University Library, Wiley Online Library on [22/09/2026]. See the Terms and Conditions (https://onlinelibrary.wiley.com/terms-and-conditions) on Wiley Online Library for rules of use; OA articles are governed by the applicable Creative Commons License

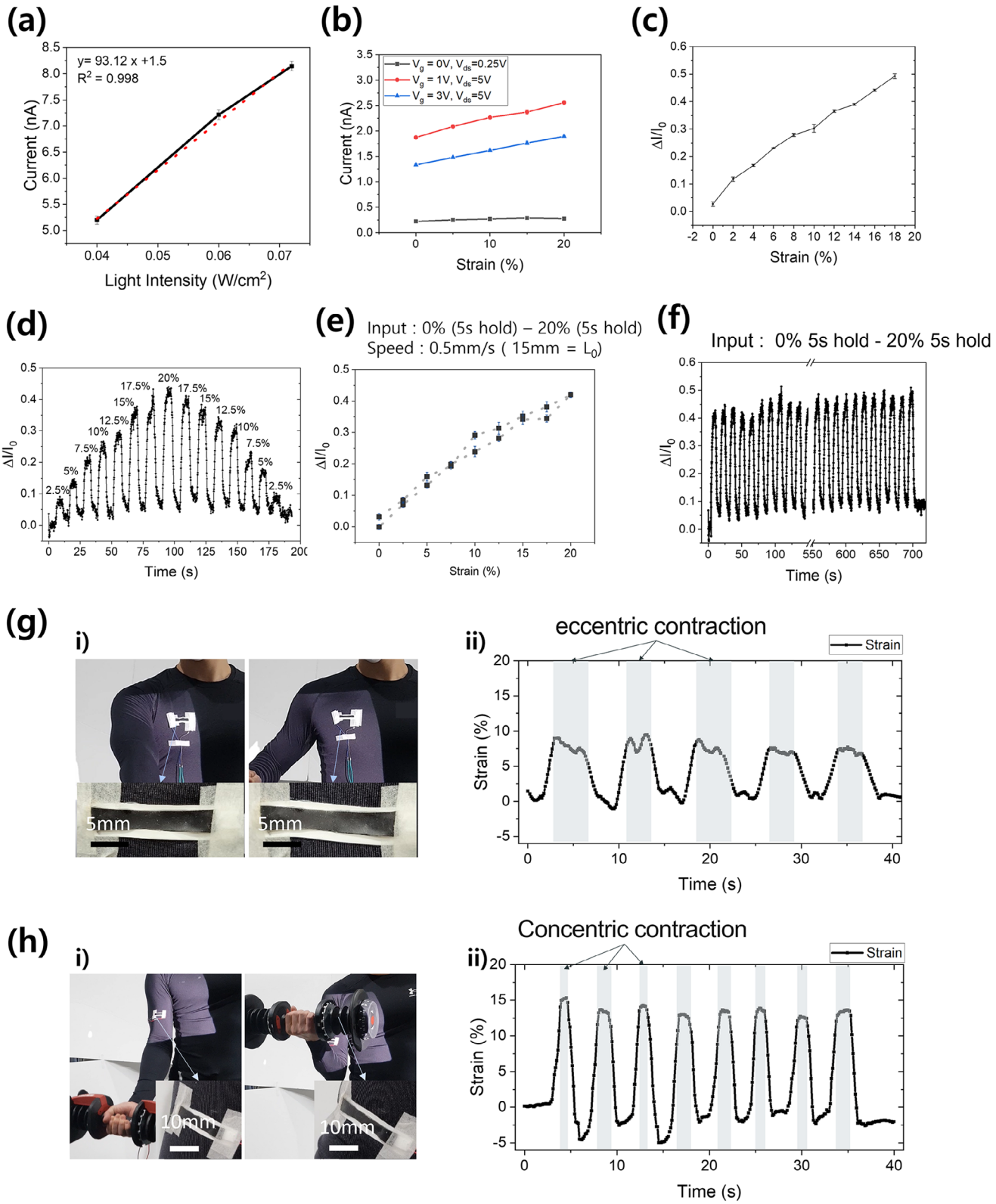


FIGURE 5 | Sensor characteristics and their application results: (a,b) MoS_2 LD layer response without PT layer. (a) MoS_2 phototransistor current response for light intensity from solar illuminator. (b) MoS_2 phototransistor current output with different gate and source-drain voltage input. Gate voltage with 1 V and source-drain voltage with 5 V show the best performance. Application of developed strain sensor to structural health monitoring. (c) Result of sensor characterization within a small strain range. The experiment was conducted to measure the detection limit of the sensor. (d) Integrated sensor responses to input step strain with a gap of 2.5% and 5 s of holding, (e) Response to input strain in the range of $\varepsilon = 0\%–20\%$. (f) Integrated sensor response of a stability test: Strain input with 5 s holds with $\varepsilon = 0\%$ and 20% for 100 cycles. (g) Photographic image of integrated sensor and experimental results of integrated strain sensors on the human body. (i) Photographic image of attached sensor on pectorals. (ii) Experimental results of for the seated chest press workout. (h,i) Photographic image of attached sensor on biceps muscles. (h-ii) Experimental results for the arm curl workout.

2365709x, 2026, 16, Downloaded from https://advanced.onlinelibrary.wiley.com/doi/10.1002/admt.202501979 by Korea University Library, Wiley Online Library on [22/09/2026]. See the Terms and Conditions (https://onlinelibrary.wiley.com/terms-and-conditions) on Wiley Online Library for rules of use; OA articles are governed by the applicable Creative Commons License

TABLE 1 | Comprehensive comparison of the sensing performance between the proposed MoS_2-integrated piezo-transmittance sensor and state-of-the-art wearable strain sensors.

Refs.	Type	Material	Sensitivity (G.F.)	Stretchability	Response Time	LOD	Durability (Cycles)
[29]	Resistive	AgNW-Graphene/PDMS	236	118%	83ms	—	>500
[30]	Resistive	TPU/CNT	—	0.05%–600%	75ms	0.05%	>1000
[31]	Resistive	Microporous PU fiber	9.95×10^5	120%	—	—	—
[31]	Resistive	Porous graphene foam / PEDOT:PSS	1401.5	45%		—	
[32]	Capacitive	CB/Fe_3O_4/silicone rubber	1–3	180%	78 ms /65 ms	0.25%	>9000
[31]	Capacitive	Conductive ionic gel	—	2%	Tens of ms	- 2%	—
[33]	Triboelectric	Aligned AgNW/PDMS	396.3	100%	<200 ms	—	>3000
[34]	Resistive	CNT/PDMS	430	100%	0.05s	—	—
—	Our work	CNT/PDMS	93.12 nA/(W/cm^2)	0%–30%	*0.507s*	0.73%	>100

which the entire device is embedded, preventing accumulation of biofluids on the sensor surface.

The response time was calculated by subtracting the rise/fall time of the measured response from that of the actual applied strain input. For a strain input of 20%, the response time showed a rise/fall time of approximately 0.507 and 0.236 s, respectively as shown in Figure S5. The components that determine the response time are the source meter Keithley 2400, which has a settling and response time of 100 µs, the GPIB cable with a 1 MB/s data sending speed, and the Labview software program on the computer, which has a signal trigger speed of 100 Hz. Therefore, the fastest data frequency of the entire system is ~50 Hz. However, the response time is about 0.5 s, which means that the MoS_2 thin film phototransistor itself limit the response time of 0.5 s.

Before demonstrating the practical applications of the integrated device, it is instructive to position its performance relative to state-of-the-art wearable strain sensors (Table 1). Conventional electrical sensors based on resistive, capacitive, and triboelectric mechanisms have achieved remarkable specific metrics. However, they frequently encounter fundamental trade-offs between sensitivity, stretchability, and signal stability under complex mechanical deformations. The novelty of our MoS_2-based piezo-transmittance sensor extends beyond competing on individual raw metrics. By implementing an island-serpentine architecture, we decoupled the mechanically rigid phototransistor from the highly stretchable CNT/Ecoflex functional layer. This innovative packaging preserves the high sensitivity inherent to the crack-based light modulation mechanism while simultaneously ensuring exceptional skin conformability. Furthermore, unlike traditional passive electrical sensors, the integration of the MoS_2 phototransistor leverages its intrinsic gate-tunable responsivity, offering an active approach to physical signal modulation. Consequently, this structurally and operationally decoupled design presents a highly promising platform for overcoming the limitations of conventional flexible optical sensors. The power consumption of the device was estimated from the electrical operating conditions of the MoS_2 phototransistor. Due to the high channel impedance inherent to the semiconductor, the device operates at power levels (estimated at ~12.5 nW) [28], several orders of magnitude lower than conventional metal foil strain gauges. These typically require low-impedance Wheatstone bridge circuits with relatively high excitation voltages, resulting in power consumptions around tens of milliwatts [23] (typically >30 mW). This low power characteristic is a practical advantage for wearable applications. The developed thin film-based strain sensor was tested for its suitability in a low-powered handheld muscle monitoring (HMM) device during weight training. In order to conduct the test, two specific exercises, the seated chest press as shown in Figure 5g–i and arm curl as shown in Figure 5h,i, were selected. To capture the muscle activity of the targeted muscles, sensors were attached to the pectorals and biceps muscles, respectively. The attached sensors were used to evaluate the repeated workouts of the two exercises, and the strain changes were monitored to ensure the accuracy of the exercise posture. During the seated chest press exercise, the pectoral muscles undergo eccentric contraction which causes the sensor to be stretched, as depicted in the blue region of Figure 5g-ii). When the biceps undergo concentric contraction, the strain sensor experiences stretching, as indicated by the blue region in Figure 5h-ii). On the other hand, during eccentric contraction of the biceps, the sensor returns to its initial state. In summary, the developed low-powered thin film-based strain sensor is suitable for use in HMM devices during weight training, as it provides accurate and repeatable measurements of muscle activity.

3 | Conclusion

This research aims to develop a novel wearable piezo-transmittance strain sensor package system for monitoring physical performance. By utilizing a serpentine structure for enhanced stretchability, along with MoS_2 phototransistors, the system significantly improves skin attachability and conformability, making it suitable for dynamic physical activities.

2365709x, 2026, 16, Downloaded from https://advanced.onlinelibrary.wiley.com/doi/10.1002/admt.202501979 by Korea University Library, Wiley Online Library on [22/09/2026]. See the Terms and Conditions (https://onlinelibrary.wiley.com/terms-and-conditions) on Wiley Online Library for rules of use; OA articles are governed by the applicable Creative Commons License

The sensor's dual-layer design, featuring a CNT-elastomer composite PT layer and a light detection LD layer, allows for precise measurement of optical transmittance changes under strain. By incorporating both island and serpentine structures, the sensor effectively withstands diverse deformations. MoS_2 was chosen for its exceptional light absorption properties in the visible spectrum, combined with the mechanical strength and electrical insulation provided by the polyimide substrate. Optimized fabrication conditions for the MoS_2 phototransistor enhanced its photodetection performance, particularly through careful adjustment of ALD temperature and channel length. Rigorous analysis of the serpentine design ensured the device's mechanical stability. The successful implementation of this sensor in a wearable workout monitoring system showcases its potential to accurately track physical performance during exercises such as seated bench presses and arm curls. This work not only advances the field of wearable technology but also paves the way for future research into enhanced monitoring systems that could revolutionize personal fitness and healthcare.

4 | Experimental Section/Methods

4.1 | Thin-Film Based MoS_2 Phototransistor Fabrication

First, a 4-inch silicon wafer was coated with a layer of Poly (Methyl Methacrylate) (PMMA) (495PMMA Series in Chlorobenzene, MicroChem Corp, USA). The pre-polymer PI (PI-1388, Vtec, USA) solution was then applied via spin-coating at 2000 rpm for 30 s, followed by baking (1 h at 150°C and 4 h at 260°C) to produce a flexible and thin PI substrate. It was repeated twice to make a thickness of approximately 20 μm. Subsequently, an alumina buffer layer (Al_2O_3) was deposited using an atomic layer deposition (ALD) technique. The gate electrode was then created using Chromium (Cr) as an adhesion layer at 30 nm and gold (Au) at 100 nm as the electrode. A gate insulator layer was fabricated using an ALD process. MoS_2 was grown based on the literature [21] using the metal-organic chemical vapor deposition (MOCVD) technique directly on an insulating SiO_2 substrate. MoS_2 was then transferred onto the target substrate via the wet transfer method utilizing a carrier film composed of polymethylmethacrylate (PMMA), which was subsequently removed through dissolution with acetone. The source and drain electrode were then deposited with the same as the gate electrode via e-beam evaporation. The source and drain electrodes were then deposited using the same material (Cr/Au) via e-beam evaporation. The active channel of the fabricated MoS_2 phototransistor was designed with a channel width of 500 μm and channel length of 20 μm, and a thickness of either 3 or 30 nm. Encapsulating MoS_2 with a high-κ Al2O3 layer was done by the ALD process as the final step.

4.2 | Fabrication of Integrated Sensor

A CNT/Ecoflex elastomer with center-focused stretchability (CEE-CFS) was produced and utilized as the piezo-transmittance layer. This center-focused stretchability design ensures that when the elastomer is subjected to tensile strain, the elongation is primarily concentrated in the central section, while the areas toward the edges remain relatively unchanged. The process for fabricating the CEE-CFS layer is illustrated in Figure S1. The CNT/isopropyl (IPA) solution was spray coated onto the donor substrate, and the Ecoflex 0030 (Smooth-On, Inc., USA) prepolymer was spin coated with 200 rpm and cured in an oven for 3 h (60°C). The center part of the PT film is masked with 3 M tape before spin coating PDMS prepolymer on top of it. After removing the tape, the PDMS was cured to create an additional layer on the side parts except for the central part. The CEE-CFS layer was then combined with the LD layer to form the integrated strain sensor, which had serpentine and island structures. The piezo-transmittance layer was cut into a serpentine structure using a femtosecond laser. The specification of the laser we used in the experiment is (SATSUMA HP2, Amplitude laser Inc., USA) with the laser parameters are laser energy 3.2 uJ, scan speed 30 mm/s, pulse duration 174 fs, pulse repetition rate 100 kHz. The femtosecond laser was used in the cutting process by utilizing a glavano scanner to enable a high-speed scanning process.

4.3 | Fabrication of Black Pigment Mixed PDMS (BM-PDMS) Layer and Integration

The BM-PDMS is produced by spin coating (100 rpm, 60 s) by mixing black pigment at 5 wt% into PDMS 10:1 prepolymer. The BM-PDMS produced here is used as a support for the entire system and to prevent the LD layer from curling and deforming during integration by fixing it. The fabricated BM-PDMS is placed on a glass coated with a PMMA layer and cut with a fiber laser in the 1550 μm wavelength region. Then, the laser-cut LD layer is fixed on the BM-PDMS supporter using Sil-poxy. The LD layer and PT layer need an additional layer to provide a gap between the LD layer and PT layer, as any friction or contact between them will hinder their movement each other. A synthetic grease containing polytetrafluoroethylene (PTFE) nanoparticles (Super Lube Multi-Purpose Synthetic Grease, Synco Chemical Corp.) was applied as the interfacial lubricant. This specific grease possesses highly non-volatile properties and maintains rheological stability across a broad temperature range (−43°C to 232°C), preventing it from drying out or evaporating during continuous mechanical deformation. The BM-PDMS layer is cut into a window shape to provide a gap, which can block the light entering the side while separating the movement between the LD layer and PT layer, so the layer and the LD layer are attached. During the fabrication process, the light-blocking pigment particles are cross-linked and embedded within the chemically inert PDMS matrix. This cross-linked network prevents any environmental leaching, oxidation, or optical degradation of the pigments. Then attach the PT layer to create an integrated strain sensor. The overall process described here is depicted on Figure S2b–f.

4.4 | Illumination Conditions and Optical Setup

To accurately evaluate the optomechanical response of the flexible piezo-transmittance sensor, optoelectronic measurements were conducted under a tightly controlled illumination setup. A visible-range (λ = 400–800 nm) solar illuminator (LAX-C100 Xenon light source, Asahi Spectra Co., Ltd., Japan) was utilized to simulate a consistent ambient light environment. The light source was positioned at a vertical distance of 100 mm directly above the

2365709x, 2026, 16, Downloaded from https://advanced.onlinelibrary.wiley.com/doi/10.1002/admt.202501979 by Korea University Library, Wiley Online Library on [22/09/2026]. See the Terms and Conditions (https://onlinelibrary.wiley.com/terms-and-conditions) on Wiley Online Library for rules of use; OA articles are governed by the applicable Creative Commons License

device surface, providing a calibrated optical power density in the range of approximately 20–50 mW/cm^2.

The illumination was fixed at a perpendicular angle (normal incidence) throughout the experiments. Since the target application relies on diffused ambient light, this fixed perpendicular geometry was strategically employed to standardize the measurement conditions, thereby strictly isolating the strain-induced transmittance changes in the functional layer from any external angular variations. Furthermore, the inherent spectral dependence and broadband visible photoresponsivity of the MoS_2 phototransistor layer (e.g., peak responsivities at 520 nm and 630 nm) follow the well-established characteristics reported in our previous work [22]. By utilizing this standardized broadband illumination setup, the high reproducibility and reliability of the strain-dependent photocurrent measurements were guaranteed.

4.5 | Finite Element Analysis Boundary Conditions

Finite element analysis was performed using COMSOL Multiphysics to evaluate the strain distribution within the island–serpentine structure under applied deformation. A symmetric boundary condition was imposed along the central axis of the island region, and a prescribed displacement was applied at the opposite end of the film to generate a uniaxial tensile strain. The magnitude of the external displacement was chosen such that the maximum volumetric strain in the serpentine interconnects matched the range of externally applied strain used in the experiments, consistent with Figure S3. Out-of-plane displacement was constrained to enforce in-plane stretching. Perfect bonding was assumed at all interfaces between the Al_2O_3 layer and the polyimide substrate, as well as between the serpentine interconnects and the rigid island regions. A static structural analysis was performed, and a relatively coarse mesh was used in the large planar regions, while a fine tetrahedral mesh was employed in the serpentine interconnects to resolve the high stress gradients and avoid interpolation errors at the interconnect–island interfaces.

Acknowledgements

This work was supported by the National Research Foundation of Korea (NRF) grant funded by the Korea government(MSIT) (No. 2021R1A2C3008742), Ministry of Culture, Sports and Tourism, and Korea Creative Content Agency (Project Number: R2021040018), and the Technology Innovation Program (00144157, Development of Heterogeneous Multi-Sensor Micro-System Platform) funded By the Ministry of Trade, Industry & Energy (MOTIE, korea).

Conflicts of Interest

The authors declare no conflicts of interest.

Data Availability Statement

The data that support the findings of this study are available from the corresponding author upon reasonable request.

References

1. M. S. Kim, Y. Lee, J. Ahn, et al., "Skin-like Omnidirectional Stretchable Platform with Negative Poisson's Ratio for Wearable Strain–Pressure Simultaneous Sensor," *Advanced Functional Materials* 33 (2023): 1.

2. Y. Jung, J. Choi, W. Lee, J. S. Ko, I. Park, and H. Cho, "Irregular Microdome Structure-Based Sensitive Pressure Sensor Using Internal Popping of Microspheres," *Advanced Functional Materials* 32 (2022): 1.

3. A. Abramson, C. T. Chan, Y. Khan, et al., "A Flexible Electronic Strain Sensor For The Real-Time Monitoring of Tumor Regression," *Science Advances* 8 (2022): 6550.

4. S. A. Dual, B. L. Zambrano, S. Sündermann, et al., "Continuous Heart Volume Monitoring by Fully Implantable Soft Strain Sensor," *Advanced Healthcare Materials* 9 (2020): 2000855, https://doi.org/10.1002/adhm.202000855.

5. S. Lin, S. Hu, W. Song, et al., "An Ultralight, Flexible, and Biocompatible all-fiber Motion Sensor for Artificial Intelligence Wearable Electronics," *npj Flexible Electronics* 6 (2022): 27, https://doi.org/10.1038/s41528-022-00158-8.

6. Y. Jeong, J. Gu, J. Byun, et al., "Ultra-Wide Range Pressure Sensor Based on a Microstructured Conductive Nanocomposite for Wearable Workout Monitoring," *Advanced Healthcare Materials* 10 (2021): 2001461, https://doi.org/10.1002/adhm.202001461.

7. M. Amjadi, K.-U. Kyung, I. Park, and M. Sitti, "Stretchable, Skin-Mountable, and Wearable Strain Sensors and Their Potential Applications: A Review," *Advanced Functional Materials* 26 (2016): 1678–1698, https://doi.org/10.1002/adfm.201504755.

8. V. Sanchez, C. J. Walsh, and R. J. Wood, "Textile Technology for Soft Robotic and Autonomous Garments," *Advanced Functional Materials* 31 (2021): 2008278, https://doi.org/10.1002/adfm.202008278.

9. H. Kim, Y. T. Kwon, H. R. Lim, J. H. Kim, Y. S. Kim, and W. H. Yeo, "Recent Advances in Wearable Sensors and Integrated Functional Devices for Virtual and Augmented Reality Applications," *Advanced Functional Materials* 31 (2021): 1.

10. Z. Zhang, T. He, M. Zhu, et al., "Deep Learning-enabled Triboelectric Smart Socks for IoT-based Gait Analysis and VR Applications," *npj Flexible Electronics* 4 (2020): 29, https://doi.org/10.1038/s41528-020-00092-7.

11. Q. Zhai and Y. Yang, "Highly Stretchable Variable-Transmittance Skin for Ultrasensitive and Wearable Strain Sensing," *Advanced Materials Technologies* 2 (2017): 1700161, https://doi.org/10.1002/admt.201700161.

12. J. Gu, D. Kwon, J. Ahn, and I. Park, "Wearable Strain Sensors Using Light Transmittance Change of Carbon Nanotube-Embedded Elastomers with Microcracks," *ACS Applied Materials & Interfaces* 12 (2020): 10908–10917, https://doi.org/10.1021/acsami.9b18069.

13. J. Gu, Y. Jung, J. Ahn, et al., "Auxetic Kirigami Structure-Based Self-Powered Strain Sensor with Customizable Performance Using Machine Learning," *Nano Energy* 130 (2024): 110124, https://doi.org/10.1016/j.nanoen.2024.110124.

14. S. Pak, Y. Cho, J. Hong, et al., "Consecutive Junction-Induced Efficient Charge Separation Mechanisms for High-Performance MoS_2 /Quantum Dot Phototransistors," *ACS Applied Materials & Interfaces* 10 (2018): 38264–38271, https://doi.org/10.1021/acsami.8b14408.

15. H. Xu, J. Wu, Q. Feng, N. Mao, C. Wang, and J. Zhang, "Flexible and Stretchable Electronics: From Materials to Devices," *Nature Communications* 10 (2014): 2300.

16. N. Huo and G. Konstantatos, "Recent Progress and Future Prospects of 2D-Based Photodetectors," *Advanced Materials* 30 (2018): 1, https://doi.org/10.1002/adma.201801164.

17. M. Long, P. Wang, H. Fang, and W. Hu, "Progress, Challenges, and Opportunities for 2D Material Based Photodetectors," *Advanced Functional Materials* 29 (2019): 1803807, https://doi.org/10.1002/adfm.201803807.

2365709x, 2026, 16, Downloaded from https://advanced.onlinelibrary.wiley.com/doi/10.1002/admt.202501979 by Korea University Library, Wiley Online Library on [22/09/2026]. See the Terms and Conditions (https://onlinelibrary.wiley.com/terms-and-conditions) on Wiley Online Library for rules of use; OA articles are governed by the applicable Creative Commons License

18. A. Taffelli, S. Dirè, A. Quaranta, and L. Pancheri, "MoS2 Based Photodetectors: A Review," *Sensors* 21 (2021): 2758, https://doi.org/10.3390/s21082758.

19. J. H. Appel, D. O. Li, J. D. Podlevsky, et al., "Low Cytotoxicity and Genotoxicity of Two-Dimensional MoS_2 and WS_2," *ACS Biomaterials Science & Engineering* 2 (2016): 361–367, https://doi.org/10.1021/acsbiomaterials.5b00467.

20. O. Lopez-Sanchez, D. Lembke, M. Kayci, A. Radenovic, and A. Kis, "Ultrasensitive Photodetectors Based on Monolayer MoS_2," *Nature Nanotechnology* 8 (2013): 497–501, https://doi.org/10.1038/nnano.2013.100.

21. K. Kang, S. Xie, L. Huang, et al., "High-Mobility Three-Atom-Thick Semiconducting Films with Wafer-Scale Homogeneity," *Nature* 520 (2015): 656–660, https://doi.org/10.1038/nature14417.

22. I. Lee, C. Park, T. S. Kim, et al., "Water-Stable and Photo-Patternable Siloxane-Encapsulated Upconversion Nanoparticles toward Flexible near-Infrared Phototransistors," *Advanced Optical Materials* 11 (2023): 2202469, https://doi.org/10.1002/adom.202202469.

23. D. Feili, M. Marschibois, S. Saremi, and H. Seidel, "Flexible Strain Gauge Sensors With Long-Term Stability And Low Power Consumption For Self-Sufficient Sensor Systems," *Procedia Engineering* 47 (2012): 782–785.

24. Y. Yang, Z. Liu, K. Shu, L. Li, and J. Li, "Flexible and Stretchable Strain Sensors Based on Conductive Nanomaterials for Human Motion Monitoring," *Advanced Materials Interfaces* 8 (2021): 1.

25. Y. J. Park, B. K. Sharma, S. M. Shinde, et al., "All MoS 2 -Based Large Area, Skin-Attachable Active-Matrix Tactile Sensor," *ACS Nano* 13 (2019): 3023–3030, https://doi.org/10.1021/acsnano.8b07995.

26. T. Widlund, S. Yang, Y. Y. Hsu, and N. Lu, "Stretchability and Compliance of Freestanding Serpentine-Shaped Ribbons," *International Journal of Solids and Structures* 51 (2014): 4026–4037, https://doi.org/10.1016/j.ijsolstr.2014.07.025.

27. Y. Q. Yang, Y. Duan, P. Chen, et al., "Realization of Thin Film Encapsulation by Atomic Layer Deposition of Al_2 O_3 at Low Temperature," *The Journal of Physical Chemistry C* 117 (2013): 20308–20312, https://doi.org/10.1021/jp406738h.

28. M. F. Khan, M. W. Iqbal, M. Z. Iqbal, M. A. Shehzad, Y. Seo, and J. Eom, "Photocurrent Response of MoS_2 Field-Effect Transistor by Deep Ultraviolet Light in Atmospheric and N_2 Gas Environments," *ACS Applied Materials & Interfaces* 6 (2014): 21645–21651, https://doi.org/10.1021/am506716a.

29. R. Wang, X. Li, and T. Chen, "Resistive Flexible Strain Sensor based on AgNWs-Gr-PDMS for Wearable Electronics," *AIP Advances* 14 (2024): 055028, https://doi.org/10.1063/5.0211831.

30. H. Li, J. Chen, X. Chang, et al., "A Highly Stretchable Strain Sensor with both an Ultralow Detection Limit and an Ultrawide Sensing Range," *Journal of Materials Chemistry A* 9 (2021): 1795–1802, https://doi.org/10.1039/D0TA10990H.

31. H. Song, "Self-Powered Strain Sensing System: A Cutting-Edge Review Paving the Way for Autonomous Wearable Electronics," *Polymers* 17 (2025): 3256, https://doi.org/10.3390/polym17243256.

32. X. Guo, W. Hong, T. Zhang, et al., "Highly Stretchable, Responsive Flexible Dual-Mode Magnetic Strain Sensor," *Advanced Materials Technologies* 8 (2023): 2201439, https://doi.org/10.1002/admt.202201439.

33. Y. Ye, J. Ning, Y. Meng, et al., "Flexible and Sensitive Triboelectric Nanogenerator Strain Sensors Made of Semi-Embedded Aligned Silver Nanowires," *Advanced Electronic Materials* 11 (2025): 2400426, https://doi.org/10.1002/aelm.202400426.

34. S. Xu, X. Xiao, and J. Chen, "Stretchable fiber Strain Sensors for Wearable Biomonitoring," *National Science Review* 11 (2024): nwae173, https://doi.org/10.1093/nsr/nwae173.

Supporting Information

Additional supporting information can be found online in the Supporting Information section.

Supporting File: admt71018-sup-0001-SuppMat.docx.

2365709x, 2026, 16, Downloaded from https://advanced.onlinelibrary.wiley.com/doi/10.1002/admt.202501979 by Korea University Library, Wiley Online Library on [22/09/2026]. See the Terms and Conditions (https://onlinelibrary.wiley.com/terms-and-conditions) on Wiley Online Library for rules of use; OA articles are governed by the applicable Creative Commons License